Journal of the Korean Ceramic Society (2022) 59:578–588
https://doi.org/10.1007/s43207-022-00189-x

ORIGINAL ARTICLE

Investigation of structural phase transition, Curie temperature and energy storage density of $Ba_{0.97}Ca_{0.03}Ti_{1-x}Sn_xO_3$ electroceramics

Pravin S. Kadhane[1] · Bharat G. Baraskar[1] · Tulshidas C. Darvade[1] · Onkar A. Ramdasi[1] · Md. Samsuzzaman[1] · Rahul C. Kambale[1]

Received: 5 October 2021 / Revised: 8 January 2022 / Accepted: 13 January 2022 / Published online: 17 February 2022

Abstract

Three different measurement methods to determine the structural phase transitions and Curie temperature of $Ba_{0.97}Ca_{0.03}Ti_{1-x}Sn_xO_3$ (BCTS, $x = 0.025$, and 0.035 mol). electroceramics are discussed. At room temperature, both compositions reveal the tetragonal perovskite lattice symmetry as evidenced by X-ray diffraction, temperature-dependent dielectric constant and Raman active modes. The temperature-dependent dielectric study reveals $T_{R\text{-}O}$ at − 60 °C, $T_{O\text{-}T}$ at 14 °C, $T_{T\text{-}C}$ at 126 °C for composition $x = 0.025$ and $T_{R\text{-}O}$ at − 50 °C, $T_{O\text{-}T}$ at 20 °C, $T_{T\text{-}C}$ at 118 °C for composition $x = 0.035$. To evident the structural changes happening at phase transitions as well as Curie temperature the variation of polarization concerning temperature is investigated which supports the temperature-dependent dielectric and Raman spectroscopy studies. The room temperature recoverable energy storage density and efficiency of BCTS are calculated by the integral area of the polarization–electric field (P-E) hysteresis loop. The observed recoverable energy storage density is 21.80 mJ/cm^3 and 32.40 mJ/cm^3 with the efficiency of 43.58% and 52.25% for composition $x = 0.025$ and 0.035 mol., respectively. These results are having practical importance, due to the higher recoverable energy storage density and efficiency with moderate Curie temperature compared to the pure $BaTiO_3$. Thus, it can be used as a promising novel and environmentally friendly, lead-free material, for different applications in low carbon vehicles, renewable energy technologies, integrated circuits, and for the high-temperature aerospace sector.

Keywords $BaTiO_3$ · Ferroelectrics · Curie temperature · Raman spectroscopy · Phase transition · Energy storage density

✉ Rahul C. Kambale
rckambale@gmail.com; rck@physics.unipune.ac.in

[1] Present Address: Department of Physics, Savitribai Phule Pune University, Pune 411 007, Maharashtra, India

1 Introduction

The Curie temperature (T_c) at which spontaneous polarization of ferroelectrics starts to cease and the ferroelectric phase becomes paraelectric plays an important role to decide their operating temperature range for practical applications in multifunctional devices. At lower temperature, rhombohedral (< − 90 °C) and orthorhombic (− 90 °C to 5 °C) phase of $BaTiO_3$ material have low symmetry; while at a higher temperature, tetragonal (5 °C to 120 °C) and in cubic phase (>120 °C) it tends toward higher symmetry. The change of symmetry and phase transition in $BaTiO_3$ is driven by both Ti and O atoms shifting along the c axis in one direction and Ba atom in the opposite direction results in a change in dipole moment and thus polarization [1]. The change of symmetry can be driven by temperature, pressure, chemical composition, electric field, etc. With the change in temperature an inconsistency is observed in dipole moment, symmetry of unit cell, specific heat capacity, dielectric permittivity and thermal expansion at the structural transition which can be utilized to detect phase transition temperature in the material. $BaTiO_3$ is the widely studied material that undergoes three polymorphic structural transitions as rhombohedra (R) to orthorhombic (O) at − 90 °C, orthorhombic (O) to tetragonal (T) at 5 °C and tetragonal (T) to Cubic (C) at 120 °C. Among these rhombohedral, orthorhombic and tetragonal phases are the non-centrosymmetric having polarization along [111], [011], [001] axis respectively and the cubic phase is centrosymmetric with no dipole moment as shown in Fig. 1a [2–5].

Multilayer ceramics capacitors (MLCC), sonar, transducer, and actuators need stable capacitance and polarization with large spam of temperature range to make it convenient for practical applications. Because the change in temperature changes the polarization in ferroelectric material, thus the temperature decides the upper and lower temperature limits for application. Most of the electronic components made up of $BaTiO_3$ are used for applications having temperatures ranging from room temperature to half of its Curie temperature, so it is prime important to know the T_c of such materials [2, 6]. Furthermore, the ABO_3 structured alkaline-bismuth-titanate-based materials ($Bi_{0.5}Na_{0.5}TiO_3$, $Bi_{0.5}K_{0.5}TiO_3$) show good dielectric and ferroelectric properties than $BaTiO_3$. But the volatility of alkaline-bismuth-titanate-based materials during sintering hampers the stability and thus the application of these materials over the wide temperature range. As compared to other lead-free materials the $BaTiO_3$ gives the stable dielectric, ferroelectric and piezoelectric with low Curie temperature (120 °C). Thus, with appropriate substitution of Ca^{2+}, Zr^{4+}, Sn^{4+}, Hf^{4+} in $BaTiO_3$ helps to improve the dielectric, ferroelectric and piezoelectric properties of Pure $BaTiO_3$ [7]. For Ca^{2+} and Sn^{4+} substituted $BaTiO_3$ ceramics we reported the O-T phase co-existence with $d_{33} = 287$ pC/N and $d^*_{33} = 505$ pm/V and $T_c \sim 126$ °C [8]. In this study, we analyzed that, the Curie temperature and structural phase transitions from a non-centrosymmetric state to a centrosymmetric state is an important aspect of the ferroelectrics before employing for further application. The Curie temperature and structural transition can be determined by six different temperature-dependent characterization techniques such as (1) X-ray diffraction, (2) dielectric constant measurement, (3) Raman spectroscopic study, (4) polarization (5) differential scanning calorimetric (DSC) curve and (6) up-conversion photoluminescence [7–10]. Determination of Curie temperature by a temperature-dependent dielectric constant is mostly reported. But, to evident the value of T_c apart from temperature-dependent dielectric constant measurement other approaches should be used, which we have done in this work. We explore the determination of Curie temperature by temperature-dependent dielectric constant measurement and confirm it with temperature-dependent Raman spectroscopy and P-E hysteresis loop.

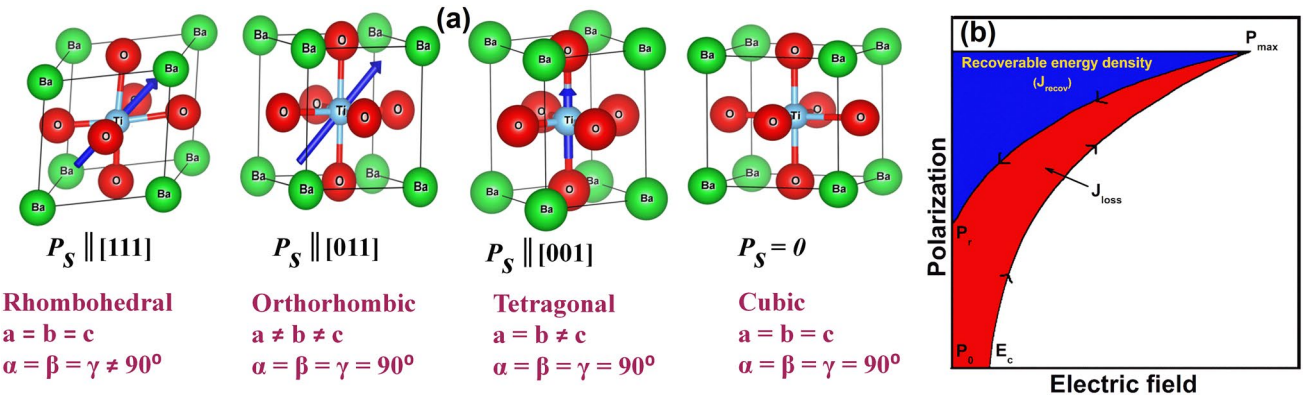

Fig. 1 **a**–**b**: (**a**) Unit cell Structure with polarization axis in rhombohedral, orthorhombic, tetragonal and cubic unit cell. **b** Demonstration of recoverable energy density and energy loss in P-E loop

Energy storage density is an important aspect in fast-growing compact and commercially available capacitors in pulsed power applications, high-power microwave systems and power electronics devices. The remnant polarization (P_r) maximum polarization (P_{max}) and break-down strength (BDS) of dielectric material are the important parameters to consider the material for energy storage density. The demonstration of recoverable energy density and loss in energy in a dielectric material is shown in Fig. 1b. There are two possible probabilities to enhance the recoverable energy storage density. One is, Low P_r value and high P_{max} which increase the difference between P_r and P_{max} and the other is to improve the BDS. Break down strength is the strength of material up to which it acts as dielectric/ferroelectric and above the BDS it becomes a conductor for an applied electric field. The creation of appropriate oxygen vacancies in dielectric material by suitable substituents acts as electron trap sites and once the electron trap levels become deeper it results in a significant enhancement in BDS. Most of the literature available for energy storage density is for the thin film capacitors and very little literature is available for the bulk ceramic capacitors [11, 12]. The substitution of Sn^{4+} for Ti^{4+} in $BaTiO_3$ and (Ba,Ca)TiO_3 decreases remnant polarization (P_r), coercive field (E_c) and shift the Curie temperature peak towards lower temperature with increasing room temperature permittivity [6, 7, 13]. Barium stannate titanate ($BaTi_{1-x}Sn_xO_3$) is a binary solid solution composed of $BaTiO_3$ and $BaSnO_3$. The substitution of higher ionic radii Sn^{4+} (0.69 Å) ion for the lower ionic radii Ti^{4+} (0.60 Å) ion in $BaTiO_3$ leads to a decrease in the ferroelectric property [7, 13]. The reduction of P_r, E_c, and J_{loss} due to substituting Sn^{4+} for the Ti^{4+}-site of (Ba,Ca)$(Ti_{1-x}Sn_x)O_3$ can lead to improved recoverable energy storage density (J_{recov}) and energy storage efficiency (η) [13]. It has been reported that the substitution of Sn^{4+} enhances the diffuse phase transition and dielectric properties of the $BaTiO_3$ and (Ba,Ca)TiO_3 ceramics [6, 7, 13]. Hence, we have tried to investigate the effect of substituting Sn^{4+} for the Ti^{4+}-site of (Ba,Ca)TiO_3 for the energy storage properties along with determination and confirmation of the structural phase transition and Curie temperature of the $BaTiO_3$-based lead-free perovskite materials.

2 Experimental details

The $(Ba_{0.97}Ca_{0.03}Ti_{1-x}Sn_x)O_3$ (BCTS, $x = 0.025$ and $x = 0.035$ mol.) ceramics were prepared by conventional solid-state reaction method. $BaCO_3$ (99%), $CaCO_3$ (99%), TiO_2 (99%), and SnO_2 (99.9%) (all are AR grade from Sigma Aldrich) were used as raw material and weighted in their stoichiometric proportion. The weighted raw materials was ball milled for 24 h. in ethanol medium then dried at 80 °C for 10 h. in the oven. This dried raw material was grounded well for 1 h. and calcined at 1100 °C for 5 h. with heating and cooling rate of 2 °C/min. To attain proper homogeneity calcined powder was further grounded for 1 h. followed by ball milling for 24 h. using ethanol medium and again drying at 80 °C for 10 h. in the oven. The calcined dried powder was pelletized in the dimension of 0.8 to 1 mm thickness and 10 mm diameter and sintered at 1300 °C for 5 h. with a heating and cooling rate of 2 °C/min in an air atmosphere. The room temperature structural phase confirmation was done using an X-ray diffractometer (D8 Advanced, Bruker Inc. Germany) with CuK_α radiation ($\lambda = 1.5406$ Å). Temperature-dependent Raman measurement was performed using a He–Ne laser of 532 nm line of Raman spectroscopy (Renishaw In Via microscope Raman) and a Linkam heating–cooling stage (THMS 600). The microstructure was examined using scanning electron microscopy (JEOL-JSM 6306A, Tokyo, Japan). The dielectric permittivity (ε) as a function of temperature from −180 to 200 °C was measured at 10 kHz using an LCR meter (HIOKI- 3532–50, Nagano, Japan). The P-E hysteresis loop at various temperatures was recorded at the fixed field of 7 kV/cm at 50 Hz, using a P-E loop tracer (Marine India). The recoverable energy density and the loss in energy during the charging and discharging cycle of BCTS were calculated from the P-E loop measurement using MATLAB (R2018a) software.

3 Results and discussion

The Fig. 2a, b shows Reitveld refined X-ray diffraction patterns of $(Ba_{0.97}Ca_{0.03}Ti_{1-x}Sn_x)O_3$ for the composition $x = 0.025$ and $x = 0.035$, respectively. Both the composition shows the perovskite structure without any trace of secondary phase formation. The Rietveld refinement pattern for the composition $x = 0.025$ and $x = 0.035$ are well matched with the tetragonal structure P4mm (ICSD#168,783) lattice symmetry and goodness of fit parameters are shown in Table 1. The peculiar characteristic peaks, (002) and (200) splitting around $2\theta = 45°$ with higher intensity of (200) than (002) along with splitting of (301) and (310) around $2\theta = 75°$ with higher intensity of (310) than (301) gives supportive evidence of tetragonal structure formation as shown in Fig. 2c, d [14]. The position of the XRD peak shift to the lower 2θ value for composition $x = 0.035$ with increasing the interplanar distance between atoms, because the ionic radii of the Sn^{4+} (0.69 Å) is greater than the Ti^{4+} (0.605 Å), which generates the lattice strain due to replacement of Ti^{4+} by Sn^{4+} and confirmed from tetragonality (c/a) ratio given in Table 1 [15]. The theoretical and actual density given in Table 1, is calculated using lattice constant obtained from the Reitveld fitted XRD pattern and liquid immersion method (Archimedes principle) in xylen medium, respectively. The bulk density calculated using theoretical and actual density is 95.64%

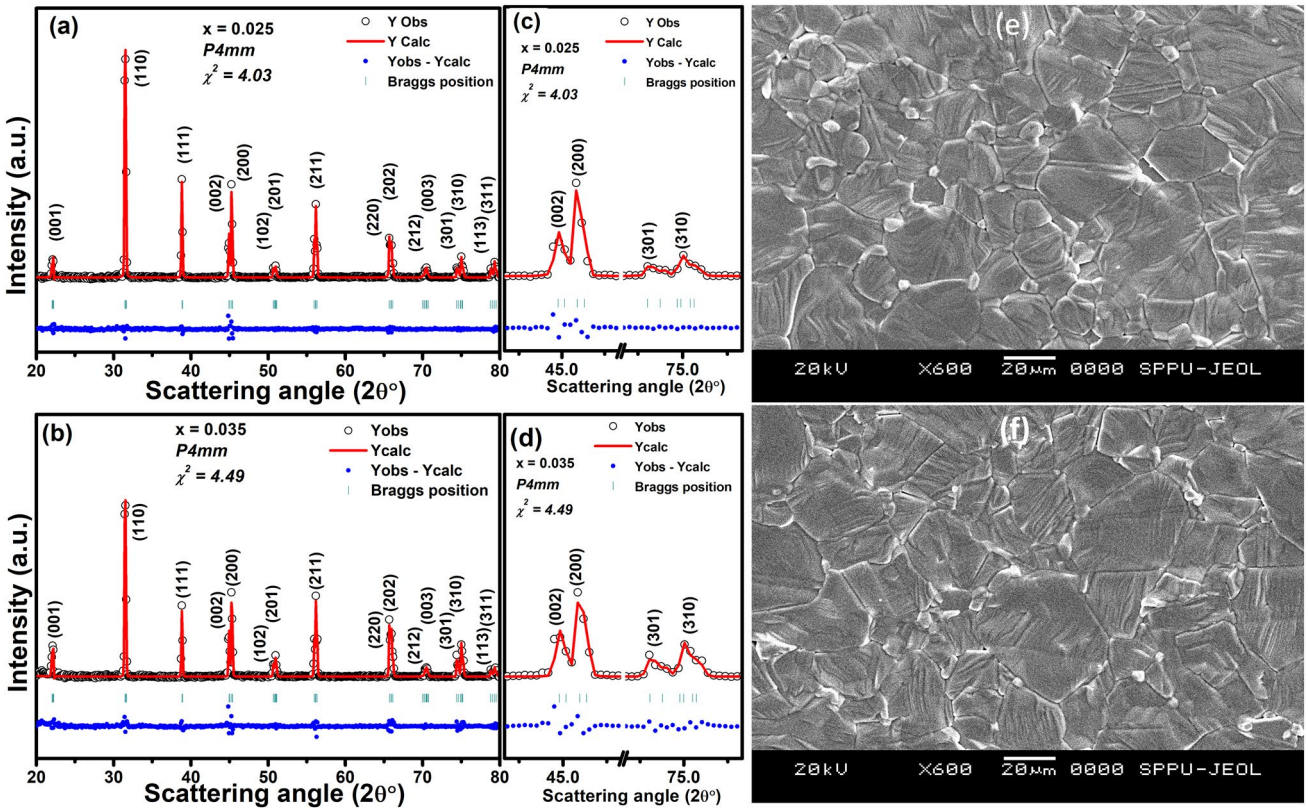

Fig. 2 **a**–**f** Rietveld refined X-ray diffraction pattern between 2θ range of 20°—80° for compositions (**a**) $x=0.025$, (**b**) $x=0.035$. Enlarged Rietveld refined X-ray diffraction pattern in the range of $2\theta=42°$—48° and $2\theta=72°$—78° for compositions (**c**) $x=0.025$, (**d**) x = 0.035. SEM micrograph for compositions (**e**) x = 0.025 and (**f**) $x=0.035$ of ($Ba_{0.97}Ca_{0.03}Ti_{1-x}Sn_x)O_3$ ceramics

and 92.69% for the composition $x=0.025$ and 0.035, respectively. The scanning electron micrographs reveal inhomogeneous grain distribution with an average grain size of 24 μm and 30 μm for the composition $x=0.025$ and $x=0.035$ as shown in Fig. 2e, f, respectively. The substitution of Sn^{4+} promotes the grain growth in BCT which increases the average grain size and thus the number of void spaces between the adjacent atoms which causes a decrease in bulk density [16].

Figure 3a, b shows the dielectric permittivity and first-order derivatives for the frequency 10 kHz in the vicinity of temperature − 180 °C to 200 °C. With an increase in the temperature both BCTS composition shows maxima at each structural transition and gives rise to three polymorphic structural phase transitions, R-O, O-T and T-C at − 60 °C, 14 °C, 126 °C for $x=0.025$ and − 50 °C, 20 °C, 118 °C for $x=0.035$, respectively. This structural transition indicates that the Sn^{4+} substitution raises the R-O and O-T transition temperature and decreases in T-C transition temperature [17]. The substitution of Sn^{4+}cation leads the BCT ceramics to decrease their Curie temperature. Because the ionic radius of Sn^{4+}cation (0.69 Å) is larger than that of the Ti^{4+}cation (0.605 Å), this substitution of Sn^{4+} for Ti^{4+} increases the bond length of Ti–O results in decreasing the bonding force of tetrahedral of B-site cation and the oxygen anion of the ABO_3 perovskite structure. As the bonding force between B–O bonds are weakening, the structural phase transition tends towards lower temperatures [18, 19]. To understand the diffuseness of the structural phase transition of both BCTS compositions, a qualitative characterization of inverse dielectric constant concerning temperature and linear plot of $\ln(T-T_m)$ versus $\ln(1/\varepsilon-1/\varepsilon_m)$ at 10 kHz was investigated. The well-known phenomenon in normal ferroelectric materials, in which dielectric permittivity follows the Curie–Weiss law above the Curie temperature is given by following equation [20]

$$\varepsilon = C/(T-T_0)(T > T_0) \quad (1)$$

where C is the Curie–Weiss constant, T_0 is the Curie–Weiss temperature and ε represents the dielectric constant. Figure 3c, d shows the inverse dielectric constant (1/ε) versus temperature at 10 kHz in the range of temperature -100 °C to 180 °C for the composition $x=0.025$ and $x=0.035$, respectively. The obtained value of Curie -Weiss constant (C) from the slop of the inverse dielectric constant and temperature is

Table 1 Structural parameters and comparison between structural phase transition temperatures measured by temperature-dependent dielectric, Raman, and polarization studies

Parameters	$X=0.025$	$X=0.035$
Lattice constant a (Å)	4.0027	4.0016
Lattice constant b (Å)	4.0027	4.0016
Lattice constant c (Å)	4.0315	4.0311
Axial ratio c/a (Tetragonality)	1.0071	1.0074
Volume of unit cell (A^3)	64.5911	64.5492
Theoretical density (g/cm^3)	5.95	5.88
Apparent density (g/cm^3)	5.69	5.45
Porosity (%)	4.36	7.31
Relative density (%)	95.64	92.69
Average grain size (μm)	24	30
T_C (°C)		
Dielectric	126	118
Raman	130	120
P-E hysteresis	130	120
χ^2	4.03	4.49
Atomic position		
x	0.0000	0.0000
Ba/Ca		
y	0.0000	0.0000
z	− 0.0403	− 0.0504
x	0.5000	0.5000
Ti/Sn		
y	0.5000	0.5000
z	0.4659	0.4179
x	0.5000	0.5000
O1		
y	0.5000	0.5000
z	0.0182	0.0231
x	0.5000	0.5000
O2		
y	0.0000	0.0000
z	0.5237	0.5533

in the order of 10^5 °C which reflects the ferroelectric structural transition. Uchino and Nomura modify Curie–Weiss law to investigate the degree of ferroelectric-paraelectric diffuse phase transition and proposed the following equation [21]

$$1/\varepsilon - 1/\varepsilon_m = \left(T - T_m\right)^{\gamma}/C' \quad (2)$$

where γ is the diffusion coefficient and C′ is the Curie constant. Generally, the value of γ for a normal ferroelectric material is 1, for an ideal ferroelectric relaxor material it is 2 and the variation of γ between 1 and 2 represents the incomplete diffused phase transition [18, 21]. The logarithmic form of Eq. (2) is given by the equation,

$$\ln\left(1/\varepsilon - 1/\varepsilon_m\right) = \gamma \ln\left(T - T_m\right) + \ln C' \quad (3)$$

The inset diagram in Fig. 3c) and Fig. 3 (d) shows the best fit to the experimental points of the linear plot of $\ln(T-T_m)$ versus $\ln(1/\varepsilon - 1/\varepsilon_m)$ at frequency 10 kHz. The value of γ obtained from the slope of plots is 1.08 and 1.19 for the composition $x=0.025$ and $x=0.035$, respectively. These values of γ show the non-relaxor ferroelectric and incomplete diffused phase transition behavior for the composition $x=0.025$ and $x=0.035$.

Temperature-dependent Raman spectra were recorded in the temperature range − 100 °C to 130 °C to ensure about the structural phase evolution is shown in Fig. 4a, b and the phase diagram based on Raman shift for peaks υ_3(LO), υ_3(TO) and υ_2(LO, TO) shown in Fig. 4c, d for composition $x=0.025$ and $x=0.035$, respectively. At − 100 °C with increasing frequency the υ_1(LO), υ_1(TO), υ_2(LO, TO), υ_4(LO), υ_3(TO) and υ_3(LO) Raman active modes observed at position 715 cm^{-1}, 525 cm^{-1}, 308 cm^{-1}, 225 cm^{-1}, 185 cm^{-1} and 168 cm^{-1}respectively [23]. Mainly the peak υ_3(LO) at 168 cm^{-1} along with two dips among υ_3(LO) and υ_3(TO) at 178 cm^{-1} as well as among υ_3(TO) and υ_4(LO) peaks at 194 cm^{-1} indicates the rhombohedral phase for $x=0.025$ and 0.035. At − 50 °C for $x=0.025$ and 0.035, the characteristic peak υ_3(LO) at 168 cm^{-1} of rhombohedral phase get disappears, while the dip among the peaks υ_3(TO) and υ_4(LO) at 194 cm^{-1} disappear as well as υ_3(TO) and other peaks show broadening. This nature of Raman spectra is an indication of the rhombohedral structure completely transforms into the orthorhombic structure. Near the temperature of 25 °C, the υ_3(TO) peak at 180 cm^{-1} disappears for both compositions which is a sign of structural change from orthorhombic to tetragonal phase. Further increase in temperature up to 130 °C for composition $x=0.025$ and 120 °C for composition $x=0.035$, υ_1(LO) peak at 715 cm^{-1} and υ_2(LO, TO) at 308 cm^{-1} are disappearing, and the entire spectrum gives only two broad peaks, υ_1(LO) at 225 cm^{-1} and υ_1(TO) at 525 cm^{-1}, which indicates the structural transition from tetragonal to cubic phase.

Figures 5a–d and 6a–d show the electric field-induced polarization (P-E) hysteresis loop at temperatures 30 °C, 60 °C, 90 °C, 130 °C and 30 °C, 60 °C, 90 °C, 120 °C for composition $x=0.025$ and $x=0.035$, respectively, at an applied electric field of 7 kV/cm. Both compositions reveal the asymmetric nature for $\pm P_r$ and $\pm E_c$ values and hence exhibit the ferroelectric imprint phenomenon [24]. When a ferroelectric material experiences high voltage or repeated pulses for a long time particularly with the increase in temperature, its polarization is not fully reversed by the application of a single voltage pulse with the opposite polarity. Thus, inadequate polarization orientation in opposite direction leads to the shift of the PE hysteresis loop along the

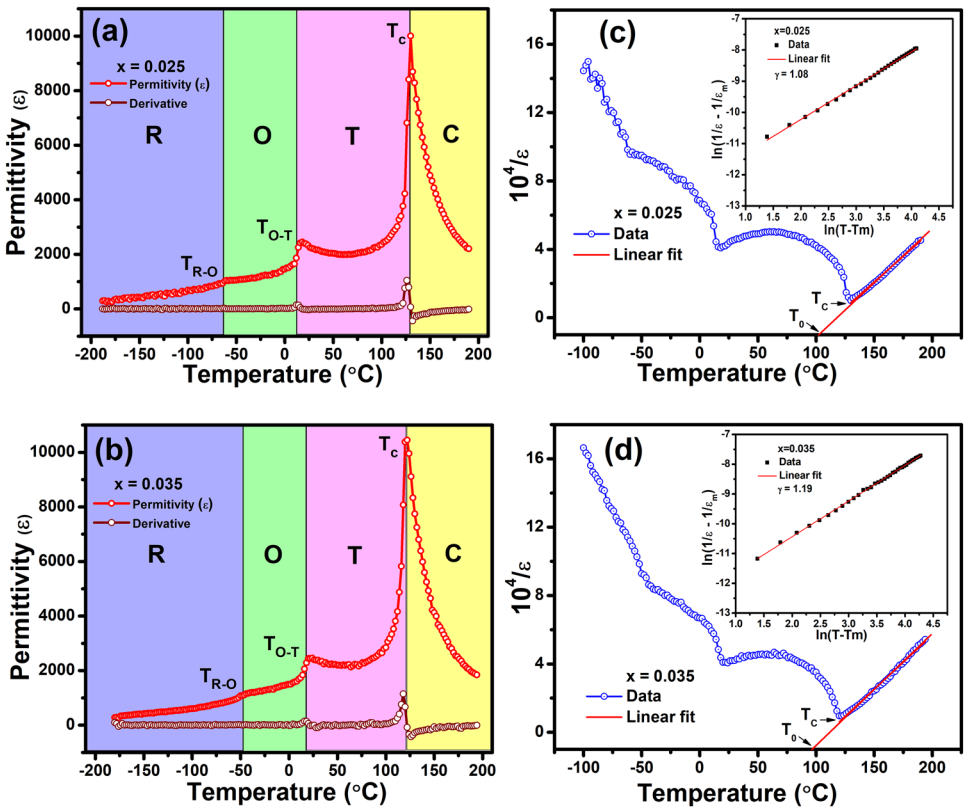

Fig. 3 **a**–**d** Temperature-dependent dielectric permittivity of $Ba_{0.97}Ca_{0.03}Ti_{1-x}Sn_xO_3$ for compositions, (**a**) x = 0.025, (**b**) 0.035. Inverse dielectric constant with respect to temperature and inset plot of $\ln(1/\varepsilon—1/\varepsilon_m)$ verses $\ln(T\text{-}T_m)$ of $Ba_{0.97}Ca_{0.03}Ti_{1-x}Sn_xO_3$ for composition (**c**) $x = 0.025$, (**d**) 0.035

electric field axis [24]. The P-E hysteresis loop shows non-linear nature up to the temperature of 90 °C for both compositions $x = 0.025$, $x = 0.035$, and becomes linear at temperature 130 °C for composition $x = 0.025$ and 120 °C for composition $x = 0.035$. This result indicates that the material shows non-linear nature until the presence of polarization in the perovskite tetragonal phase and above Curie temperature polarization due to dipole moment becomes zero, resulting in the linear nature of PE hysteresis loop. Figures 5e and 6e show spontaneous polarization and inverse permittivity concerning temperature for composition $x = 0.025$ and $x = 0.035$, respectively. The spontaneous polarization and inverse permittivity vanish at Curie temperature. While after Curie temperature the spontaneous polarization remains stable near to zero and the inverse permittivity again starts to increase with temperature. According to Landau theory; the presence of interface, hetero-phase state, and hysteresis are the required parameters for the first-order transition and change in any one of these parameters is sound to evidence the first-order transition as they are intimately linked with each other [25]. The temperature-dependent P-E measurement for composition $x = 0.025$ and $x = 0.035$ shows a decrease in polarization and hysteresis loss (energy loss) with an increase in temperature. Thus, a decrease in energy loss (hysteresis) of material from a nonlinear ferroelectric state to a linear paraelectric state is an indicator of the first-order phase transition of the synthesized material. Thus, the P-E hysteresis loop with non-linear ferroelectric tetragonal structure and linear cubic structure accomplished the Curie temperature 130 °C and 120 °C for composition $x = 0.025$ and $x = 0.035$, respectively, which is consistent with the temperature-dependent dielectric and Raman spectroscopic study [8, 26].

To know the probability in practical applications, the energy storage performances for the compositions $x = 0.025$ and $x = 0.035$ were studied as a function of an applied electric field at room temperature. The energy-storage density of the BCTS materials for composition $x = 0.025$ and $x = 0.035$ was investigated according to the schematic diagram given in Fig. 1b. The recoverable energy density (J_{recov}) stored in the dielectric material is calculated from P-E hysteresis loops using the following equations [27–29]:

$$J_{recov} = -\int_{P_m}^{P_r} Edp \tag{4}$$

where, P_r and P_m are remnant and maximum polarization values respectively, and E is the applied electric field. The obtained values for J_{recov} with above equation are 21.84 mJ/cm^3 and 32.40 mJ/cm^3 for composition x = 0.025 and x = 0.035, respectively. The loss in electrical energy (J_{loss}) due to inherent hysteresis calculated by the numerical integration of the closed area of the PE hysteresis loop is given by the equation,

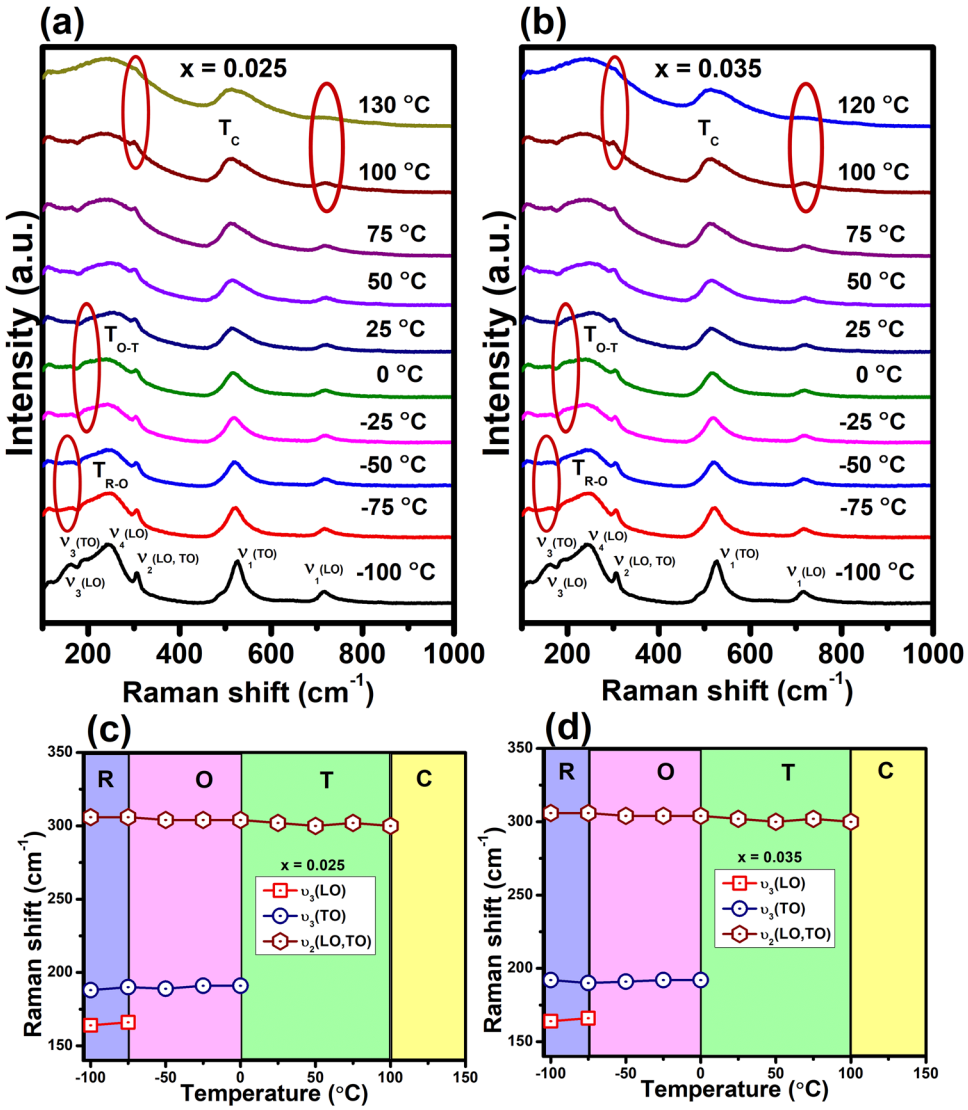

Fig. 4 **a**–**d** Temperature-dependent Raman spectra of $Ba_{0.97}Ca_{0.03}Ti_{1-x}Sn_xO_3$ for compositions, (**a**) $x=0.025$, (**b**) 0.035. Position of Raman Modes of $Ba_{0.97}Ca_{0.03}Ti_{1-x}Sn_xO_3$ for compositions (**c**) $x=0.025$, (**d**) 0.035

$$J_{\text{loss}} = \int_0^{P_r} Edp \tag{5}$$

Thus, the observed loss in electrical energy is 28.75 mJ/cm^3 and 29.6 mJ/cm^3 for the composition $x=0.025$ and $x=0.035$, respectively. The sum of electrical loss (J_{loss}) and the recoverable energy density gives the total amount of energy to charge a ferroelectric capacitor and given by the equation,

$$J_{\text{total}} = J_{\text{recov}} + J_{\text{loss}} \tag{6}$$

With the analogy of the total energy density, 50.59 mJ/cm^3 and 62 mJ/cm^3 are the energy required to charge the ferroelectric capacitors of the composition $x=0.025$ and $x=0.035$, respectively. Based on Eqs. (4) and (5), the energy storage efficiency (η) value of material can be calculated with the following equation:

$$\eta = \frac{J_{\text{recov}}}{J_{\text{recov}} + J_{\text{loss}}} \times 100 \tag{7}$$

Thus, the calculated value of efficiency from Eq. (7) are 43.58% and 52.25% for the compositions $x=0.025$ and 0.035, respectively. The increase in the efficiency from the composition $x=0.025$ to $x=0.035$ is due to the decrease in the coercive electric field with composition caused by the oxygen vacancies. Figures 5f and 6f show the change in recoverable energy density (J_{recov}), energy density loss (J_{loss}) and efficiency (η) concerning temperature. The observed values for J_{recov}, η and J_{loss} at Curie temperature for composition $x=0.025$ are 47.14 mJ/cm^3, 87.78% and 6.56 mJ/cm^3 respectively. Similarly

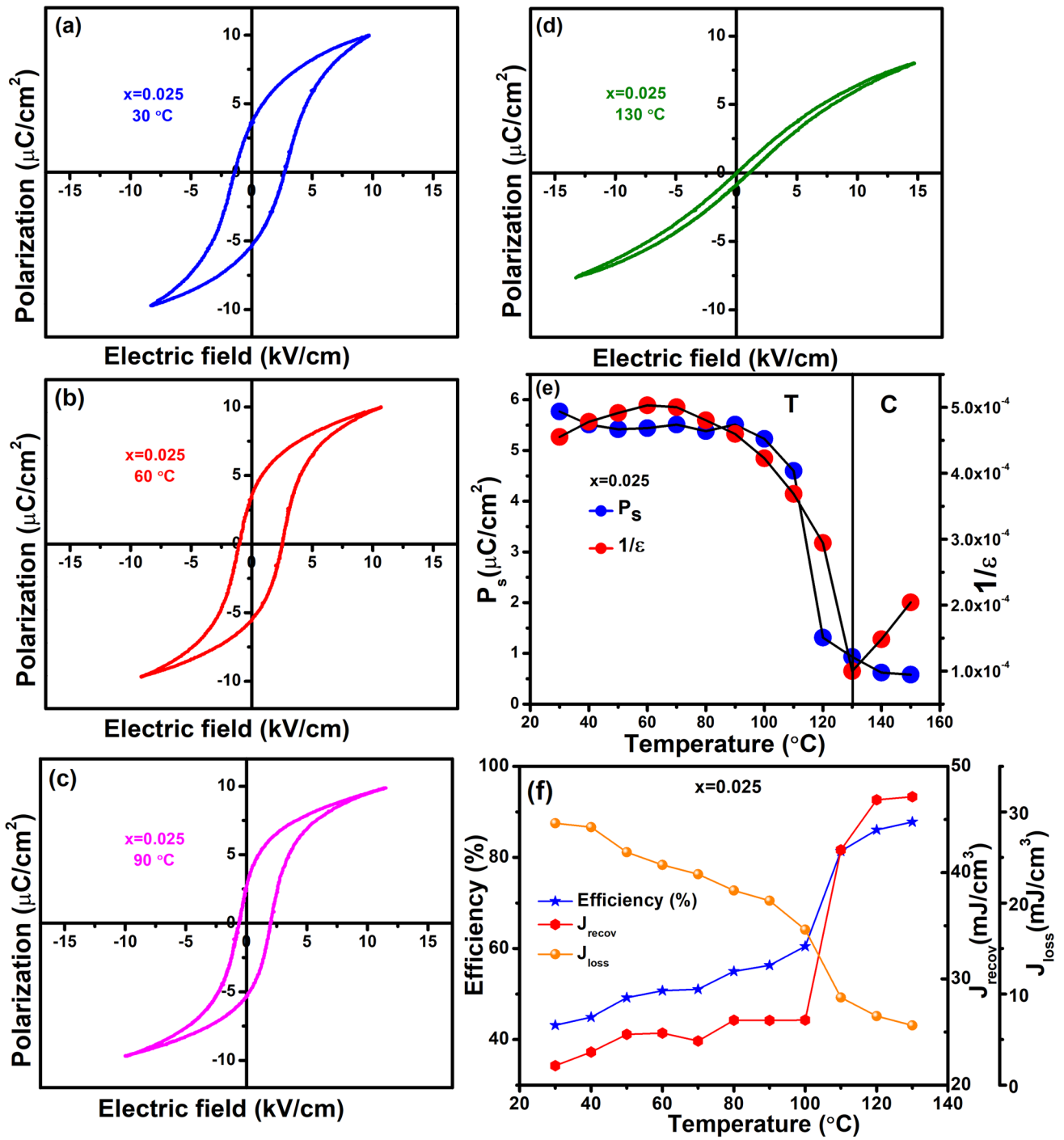

Fig. 5 **a**– **f** Polarization verses electric field loops at temperatures (**a**) 30 °C, (**b**) 60 °C, (**c**) 90 °C and (**d**) 130 °C, (**e**) variation of spontaneous polarization and inverse permittivity with respect to temperature, (**f**) temperature dependent recoverable energy density (J_{recov}), energy loss (J_{loss}) and efficiency (η) for composition $(Ba_{0.97}Ca_{0.03}Ti_{0.975}Sn_{0.025})O_3$

for composition $x=0.035$ the observed values are 66.21 mJ/cm^3, 82.59% and 13.95 mJ/cm^3 for J_{recov}, η and J_{loss}, respectively. As temperature increases the ferroelectric tetragonal structure of $Ba_{0.97}Ca_{0.03}Ti_{1-x}Sn_xO_3$ becomes cubic at 126 ºC for composition $x=0.025$ and 120 ºC for composition $x=0.035$ giving rise to slimmer PE loop results in a decrease in the remnant polarization and hysteresis loss [30]. According to Eq. (4) as remnant polarization decreases the ΔP ($\Delta P=P_{max}—P_r$) value increases, which is favorable to increase recoverable energy density (J_{recov}) along with the decrease in

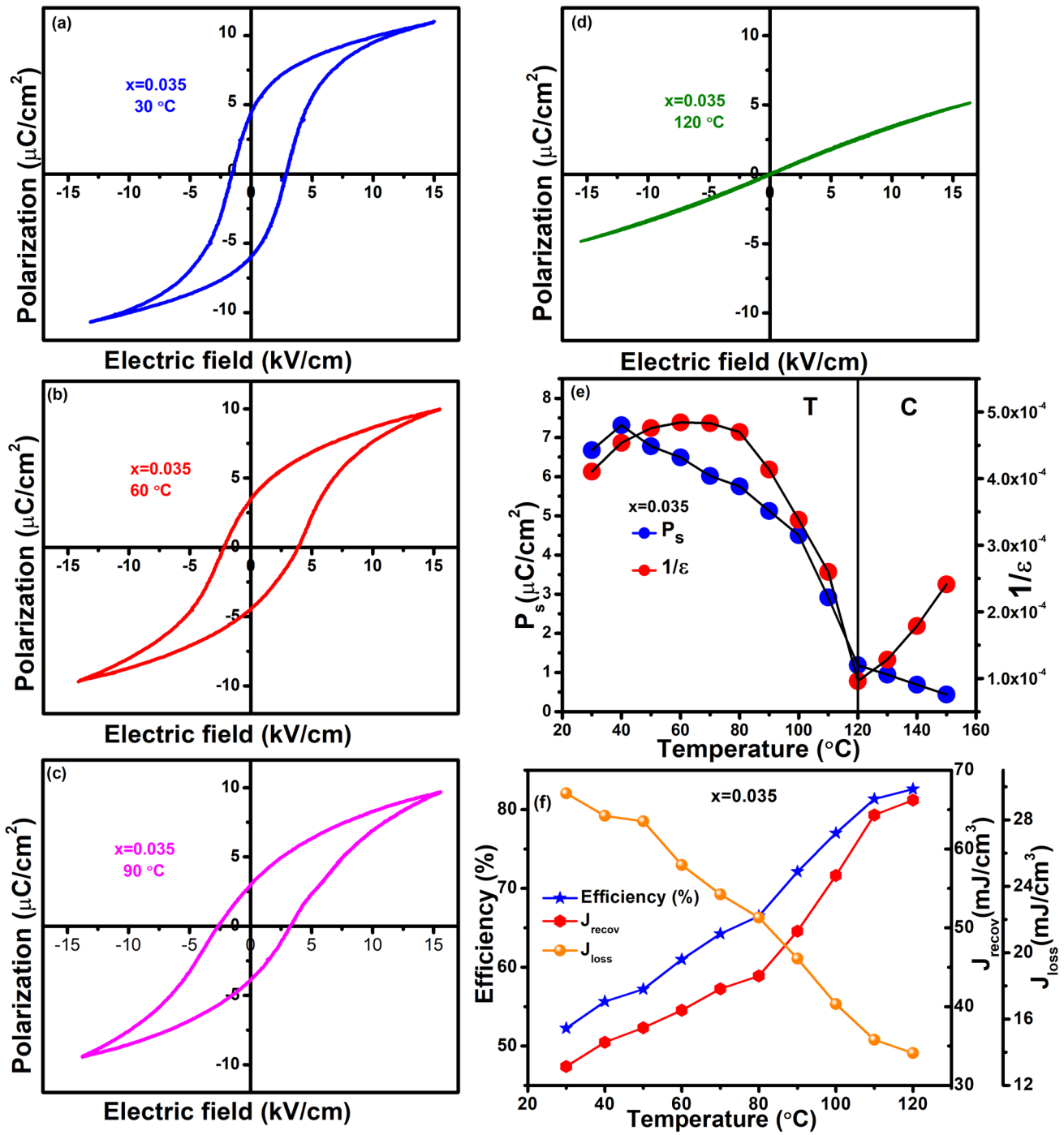

Fig. 6 **a**– **f** Polarization verses electric field loops at temperatures (**a**) 30 °C, (**b**) 60 °C, (**c**) 90 °C and (**d**) 120 °C, (**e**) variation of spontaneous polarization and inverse permittivity with respect to temperature, (**f**) temperature dependent recoverable energy density (J_{recov}), energy loss (J_{loss}) and efficiency (η) for composition $(Ba_{0.97}Ca_{0.03}Ti_{0.965}Sn_{0.035})O_3$

energy density loss (J_{loss}). The increase in J_{recov} and decrease in J_{loss} effectively increase the efficiency (η). The observed recoverable energy density, energy density loss and efficiency of BCTS material at room temperature are compared with other lead-free polymer and bulk ceramics in Table 2. With such J_{loos}, J_{reco} and efficiency (η) values, the BCTS ceramics are comparable with other lead-free ceramics for the

Table 2 Comparative chart for energy storage density parameters

Compositions	Parameters						
	P_r ($\mu C/cm^2$)	E_c (kV/cm)	J_{recov} (mJ/cm^3)	J_{loss} (mJ/cm^3)	J_{total} (mJ/cm^3)	Efficiency (η %)	Ref
$BaTiO_3$ / Polymer (composite)	3.2	25	105	61.66	166.66	63	27
0.70(PVDF)-0.30(BCZT) (Polymer)	0.20	26.42	17.01	21.56	38.56	44.10	31
$BaTiO_3$ / PVDF polymer	2.99	–	15.7	2.68	18.38	85.4	32
$(Pb_{0.96}La_{0.04}Zr_{0.60}Ti_{0.40})O_3$ (Ceramics)	27.1	11.4	36	630	666	5.36	33
$(Ba_{0.97}Ca_{0.03}Ti_{0.975}Sn_{0.025}O_3$ (Ceramics)	4.5	2.06	21.80	28.75	50.59	43.58	This work
$(Ba_{0.97}Ca_{0.03}Ti_{0.965}Sn_{0.035})O_3$ (Ceramics)	5.17	2.22	32.40	29.60	62.00	52.25	This work

energy-storage capacity and have potential application in electrostatic energy-storage devices [27, 31–33].

4 Conclusions

The $Ba_{0.97}Ca_{0.03}Ti_{1-x}Sn_xO_3$ ceramics prepared by solid-state reaction reveal the formation of tetragonal perovskite structure without a trace of any secondary phase formation. The temperature-dependent dielectric and Raman spectroscopic study gives three polymorphic structural transitions corresponding to T_{R-O}, $T_{O-T,}$ and T_{T-C}. Temperature-dependent P-E hysteresis loops provide information about the first-order ferroelectric to the paraelectric structural transition of BCTS ceramics for compositions $x = 0.025$ and 0.035. The energy storage density 21.80 mJ/cm^3 and 32.40 mJ/cm^3 with efficiency (η) of 43.58% and 52.25% of composition $x = 0.025$ and $x = 0.035$ are comparable with other lead-free ceramics for the energy-storage capacity and have potential application in electrostatic energy-storage devices. Thus, this work determines and confirms the structural phase transition and Curie temperature as well as energy storage density of the $BaTiO_3$-based lead-free perovskite materials.

Acknowledgements RCK thankfully acknowledges the Science and Engineering Research Board (SERB), Government of India (File No. EMR/2016/001750) for providing the research funds under the Extra Mural Research Funding (Individual Centric) scheme.

References

1. Ch. Eisenschmidt, H.T. Langhammer, R. Steinhausen, G. Schmidt, Ferroelectrics **432**, 103 (2012)
2. K. C. Kao, Dielectric Phenomenon in Solids with emphasis on physical concepts of electronic processes, Elsevier New York, (2004).
3. E. Chandrakala, J. P. Praveen, A. Kumar, A. R. James, D. Das, J. Am. Ceram. Soc. 99 11 3659 (2016).
4. B. Rawal, P. Dixit, N.N. Wathore, B. Praveenkumar, H.S. Panda, Bull. Mater. Sci. **43**, 82 (2020)
5. D. Shihua, S. Tianxiu, Y. Xiaojing, L. Guanghua, Ferroelectrics **402**, 55 (2010)
6. A. K. Nath, N. Medhi, Bull. Mater. Sci. 35 5 847 (2012).
7. M. Acosta, N. Novak, V. Rojas, S. Patel, R. Vaish, J. Koruza, G. A. Rossetti, J. Rödel, Appl. Phys. Rev. 4, 041305 (2017).
8. P. S. Kadhane, B. G. Baraskar, T. C. Darvade, A. R. James, R. C. Kambale, Solid State Commun. 306 113797 (2020).
9. M. A. Ansari, K. Sreenivas, Mater. Lett. 264 127294 (2020).
10. J. Wu, W. Mao, Z. Wu, Y. Jia, Mater. Lett. **166**, 75 (2016)
11. V. S. Puli, D. K. Pradhan, S. Adireddy, R. Martínez, P. Silwal, J. F. Scott, C. V. Ramana, D. B. Chrisey, R. S. Katiyar, J. Phys. D: Appl. Phys. 48 355502 (2015).
12. Y. Zhang, W. Li, W. Cao, Y. Feng, Y. Qiao, T. Zhang, W. Fei, Appl. Phys. Lett. 110, 243901 (2017).
13. S. Markovi, M. Mitri, N. Cvjeticanin, D. Uskokovic, J. Eur. Ceram. Soc. **27**, 505–509 (2007)
14. N. Chaiyo, D.P. Cann, N. Vittayakorn, Mater. Design **133**, 109 (2017)
15. M. Khan, A. Mishra, J. Shukla, P. Sharma, AIP Conference Proceedings 2100, 020138 (2019).
16. T. Hoshina, S. Hatta, H. Takeda, T. Tsurumi, Jpn. J. Appl. Phys. 57 0902BB (2018).
17. A. Kalyani, K. Brajesh, A. Senyshyn, R. Ranjan, Appl. Phys. Lett. 104 252906 (2014).
18. S. J. Kuang, X. G. Tang, l. Y. Li, Y. P. Jiang, Q. X. Liu, Scripta Materialia 61 68 (2009).
19. I. Ramovatar, S. Coondoo, N. Satapathy, Panwar. Physica B **553**, 68 (2019)
20. J.P. Praveen, K. Kumar, A.R. James, T. Karthik, S. Asthana, D. Das, Curr. Appl. Phys. **14**, 396–402 (2014)
21. K. Uchino, S. Nomura, Ferroelectr. Lett. **44**, 55–61 (1982)
22. L. Qiang, N. Li, P. Haijun, Z. Nianshun, F. Huiqing, Ceram. Int. **45**, 1676 (2019)
23. C.H. Perry, D.B. Hall, Phys. Rev. Lett. **15**, 700 (1965)
24. Hiroshi Ishiwara, journal of Nanoscience and Nanotechnology, Vol. 12, 7619–7627, 2012.
25. Y. Mnyukh, American Journal of Condensed Matter Physics 3(5) 25 142–150 (2013).
26. P. Jaita, A. Watcharapasorn, N. Kumar, D.P. Cann, S. Jiansirisomboon, Electron. Mater. Lett. **11**, 828 (2015)
27. G. Jian, Y. Jiao, Q. Meng, Z. Wei, J. Zhang, C. Yan, K. S. Moon, C.P. Wong, Communications materials, doi.org/https://doi.org/10.1038/s43246-020-00092-0.
28. F. Akram, M. Sheeraz, A. Hussain, W. Kim, T.H. Kim, C.W. Ahn, Ceram. Int. **47**, 23488–23496 (2021)

29. Y. Huang, F. Li, H. Hao, F. Xia, H. Liu, S. Zhang, J. Materiomics **5**, 385–393 (2019)
30. M. Zhoua, R. Liang, Z. Zhou, X. Dong, j. ceramint, 2019, 09, 265.
31. T. Garg, V. Annapureddy, K.C. Sekhar, D.Y. Jeong, N. Dabra, J.S. Hundal, Polym. Compos. **41**(12), 5305–5316 (2020)
32. Z. Zhang, S. Luo, S. Yu, Z. Guan, R. Sun, C.P. Wong, Mater. Des. **142**, 106–113 (2018)
33. A. Kumar, K.C.J. Raju, J. Ryu, A.R. James, Appl. Phys. A **126**, 175 (2020)